

Simultaneous Enhancement of Charge Separation and Hole Transportation in a TiO₂–SrTiO₃ Core–Shell Nanowire Photoelectrochemical System

Fei Wu, Yanhao Yu, Huang Yang, Lazarus N. German, Zhenquan Li, Jianguo Chen, Weiguang Yang,* Lu Huang, Weimin Shi, Linjun Wang,* and Xudong Wang*

Efficient charge separation and transportation are key factors that determine the photoelectrochemical (PEC) water-splitting efficiency. Here, a simultaneous enhancement of charge separation and hole transportation on the basis of ferroelectric polarization in TiO₂–SrTiO₃ core–shell nanowires (NWs) is reported. The SrTiO₃ shell with controllable thicknesses generates a considerable spontaneous polarization, which effectively tunes the electrical band bending of TiO₂. Combined with its intrinsically high charge mobility, the ferroelectric SrTiO₃ thin shell significantly improves the charge-separation efficiency ($\eta_{\text{separation}}$) with minimized influence on the hole-migration property of TiO₂ photoelectrodes, leading to a drastically increased photocurrent density (J_{ph}). Specifically, the 10 nm-thick SrTiO₃ shell yields the highest J_{ph} and $\eta_{\text{separation}}$ of 1.43 mA cm⁻² and 87.7% at 1.23 V versus reversible hydrogen electrode, respectively, corresponding to 83% and 79% improvements compared with those of pristine TiO₂ NWs. The PEC performance can be further manipulated by thermal treatment, and the control of SrTiO₃ film thicknesses and electric poling directions. This work suggests a material with combined ferroelectric and semiconducting features could be a promising solution for advancing PEC systems by concurrently promoting the charge-separation and hole-transportation properties.

Photoelectrochemical (PEC) water splitting offers a promising strategy for converting solar energy to chemical fuels.^[1–4] Among various PEC materials, titanium dioxide (TiO₂) is one of the most attractive candidates for constructing efficient and robust PEC photoanode due to its high resistance to photocorrosion, appropriate band-edge position, natural abundance, nontoxicity, and low-cost.^[5–8] However, the low

photocurrent density caused by the weak light absorption and poor charge separation currently exclude TiO₂ from developing practical PEC systems. Prevailing strategies for tuning the charge-separation ability are primarily relying on the chemistry and structure design, such as reducing the crystal size down to the same scale of charge diffusion length,^[9–11] introducing catalysts to act as charge sink,^[12–14] and doping TiO₂ with foreign elements to enhance the carrier conductivity.^[15,16] Nowadays, these chemistry and structural optimizations are approaching the apex of the charge manipulating function due to the synthesis restrictions.

For a PEC system, the charge separation is driven by the electric field in the depletion region, which is originated from the energy discontinuity at the semiconductor/electrolyte interface. Engineering the interfacial electronic band structure is the most fundamental strategy to tune the charge-separation property of a PEC device. The electronic band structure is

predominantly determined by the charge distribution along the semiconductor/electrolyte interface. Ferroelectric polarization has shown great promise in controlling the band structures and charge transport behaviors in a variety of heterojunction-based semiconductor systems, such as solar cells and field effect transistors.^[17–19] The spontaneous electric polarization could induce a considerable free charge redistribution in adjacent semiconductors, leading to the effective tuning of the width and amplitude of the depletion region. This functionality provides an unprecedented platform for fundamentally adjusting the charge-separation property of the PEC electrode beyond the limitation of chemistry and structural optimizations. Barium titanate (BTO) and lead zirconate titanate are strong ferroelectrics and have shown certain charge tuning capabilities in PEC systems.^[20–23] However, these ferroelectrics are highly insulating. These insulating materials give rise to an extra hole-transfer barrier between the semiconductor and electrolyte, which severely hinders the hole migration and thus jeopardizes the photocurrent density. A possible solution to alleviate this drawback is to replace the insulating ferroelectric with a

F. Wu, H. Yang, Z. Q. Li, Prof. J. G. Chen, Prof. W. G. Yang, Dr. L. Huang, Prof. W. M. Shi, Prof. L. J. Wang
Department of Electronic Information Materials
School of Materials Science and Engineering
Shanghai University
Shanghai 200444, China
E-mail: wgyang@shu.edu.cn; ljwang@shu.edu.cn

Y. H. Yu, L. N. German, Prof. X. D. Wang
Materials Science and Engineering
University of Wisconsin-Madison
Madison, WI 53706, USA
E-mail: xudong@engr.wisc.edu

DOI: 10.1002/adma.201701432

semiconducting material with similar permanent polarizations. Strontium titanate (STO) is an incipient ferroelectric which shows considerable electric polarization upon the interfacial stress-induced lattice distortion.^[24,25] Concurrently, STO has higher room-temperature electron mobility ($\approx 5\text{--}8\text{ cm}^2\text{ V}^{-1}\text{ s}^{-1}$) compared with TiO_2 ($\approx 0.1\text{--}4\text{ cm}^2\text{ V}^{-1}\text{ s}^{-1}$).^[26,27] These two features promise STO in developing ferroelectric PEC system with simultaneous improvement of charge separation and hole transportation. Here, we present a ferroelectric-enhanced PEC water splitting based on a TiO_2 -STO core-shell nanowire (NW) structure. The STO shell with controllable film thickness was obtained through hydrothermally converting TiO_2 NW surface to STO. After the conversion, 4.5–35 nm STO with strained interface lattice can uniformly cover the entire TiO_2 NW surface. Significantly increased charge separation and photocurrent density were achieved by the ferroelectric STO. The water-splitting performance of this PEC ferroelectric system can be effectively tuned by introducing the thermal treatment, controlling the STO shell thicknesses and altering the electric poling directions of STO.

Four different thicknesses of the STO shell were obtained by converting TiO_2 NW arrays in strontium hydroxide solution at 160 °C with the processing time between 1 and 4 h (Figure S1, Supporting Information). **Figure 1a–d** and Figure S2 (Supporting Information) show the scanning electron microscopy (SEM) images of TiO_2 NWs and TiO_2 -core-STO-shell NWs. The average lengths of all the NWs were $\approx 1.5\text{ }\mu\text{m}$. Compared to pristine TiO_2 NWs, the diameter and surface roughness of TiO_2 -STO NWs increased with the conversion time. In addition to surface conversion, there were a few nanoparticles formed at the top of NWs (**Figure 2b**), indicating a faster STO formation at the tip region. The crystal structures of pristine TiO_2 NWs and TiO_2 -STO NWs were characterized by the X-ray diffraction (**Figure 1e**). In the pristine TiO_2 NWs, two diffraction

peaks centered at 36.5° and 63.2° were detected, corresponding to the (101) and (002) crystal planes of tetragonal rutile TiO_2 (JCPDS No. 88-1175). After STO conversion, the characteristic peak of STO emerged at 32.2°, referring to STO (110) plane (JCPDS No. 35-0734). With the increase of reaction time, the peak intensities of the cubic STO and rutile TiO_2 increased and decreased, respectively, implying the continuing conversion from TiO_2 to STO.

To reveal the film thickness and surface uniformity of the STO shell, the TiO_2 and TiO_2 -STO NWs were observed using transmission electron microscopy (TEM) and scanning transmission electron microscopy (STEM) coupled with an electron energy loss spectrometer (EELS). **Figure 2a** presents a low-magnification TEM image of the pristine TiO_2 NW, demonstrating a clear rectangular shape with a diameter of $\approx 29\text{ nm}$. High-resolution TEM image (**Figure 2b**) identified a high-quality single-crystalline feature of the NW. Two sets of lattice fringes were measured with the lattice spacing of 0.29 and 0.32 nm, matching well with the (001) and (110) planes of rutile TiO_2 , respectively. **Figure 2c** shows the TEM image of the TiO_2 -STO NW prepared at 160 °C with the conversion time of 1 h. A fairly uniform STO shell covered the entire TiO_2 core. The film thickness and surface roughness of the STO shell increased with the conversion time. A maximum film thickness up to 35 nm can be obtained after 4 h conversion (**Figure S3**, Supporting Information). Based on the SEM and TEM observations, the shell thickness of 2 and 3 h samples were estimated to be 10 and 30 nm, respectively. High-resolution TEM (HRTEM) image reveals the tetragonal domain of STO lattice at TiO_2 -STO interface from the 160 °C 1 h sample (**Figure 2d**). The corresponding fast-Fourier-transform pattern (inset of **Figure 2d**) reveals that (001) plane of the STO shell is parallel to (110) plane of the TiO_2 core. As demonstrated in **Figure S4** (Supporting Information), the (110) plane of TiO_2 is parallel to the *c*-axis of TiO_2 . Meanwhile,

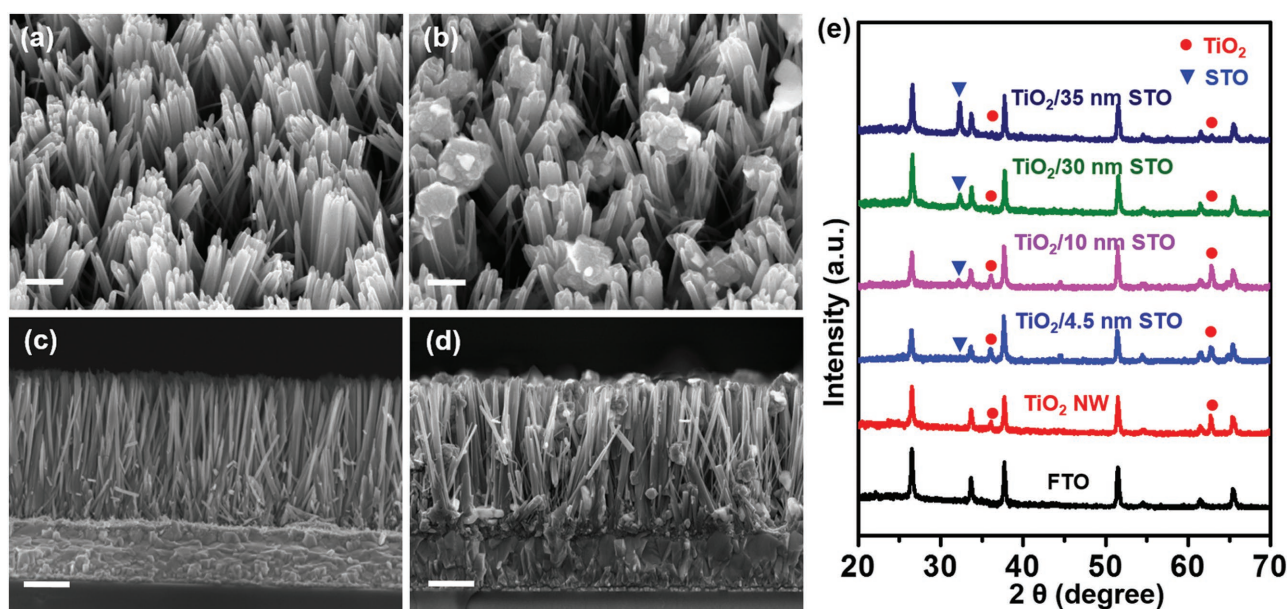


Figure 1. Morphological and compositional studies of the NW arrays. a,b) 15°-tilted view and c,d) cross-sectional SEM images of a,c) pristine TiO_2 NWs and b,d) TiO_2 core-STO shell NWs obtained after 2 h hydrothermal conversion at 160 °C. Scale bars: 200 nm (tilted-view) and 500 nm (cross-sectional). e) XRD patterns of FTO substrate, pristine TiO_2 NW array, and TiO_2 -STO core-shell NWs with four different STO shell thicknesses.

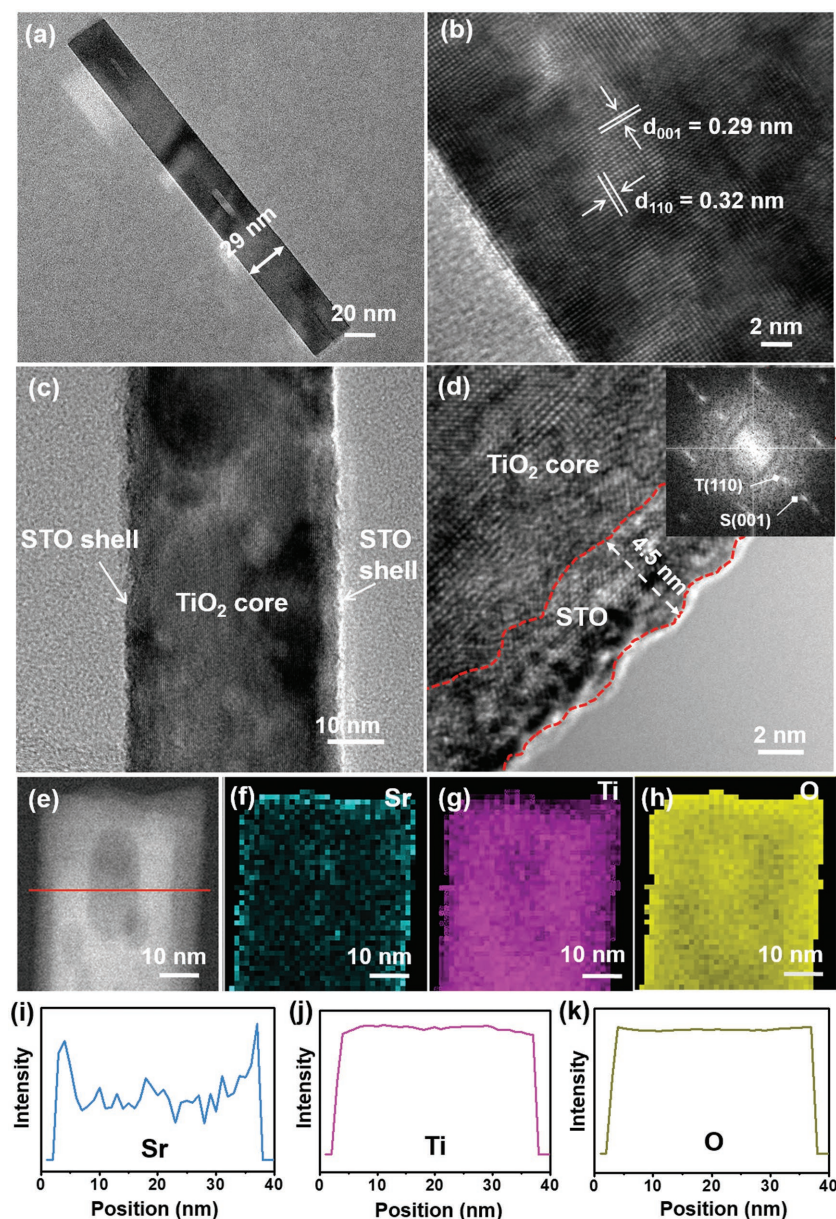


Figure 2. Structural and elemental characterizations of the TiO_2 -based NWs. a) TEM image of a single as-synthesized pristine TiO_2 NW. b) HRTEM images of the pristine TiO_2 NW confirming its single-crystallinity and rutile phase. c) TEM image of a TiO_2 -STO core-shell NW prepared at 160 °C for 1 h. d) HRTEM image of the core-shell NW along the edge showing distinct crystalline STO shell that was ≈ 4.5 nm in thickness. The inset is the corresponding FFT image. e) STEM image of the tip region of a TiO_2 -STO core-shell NW. Corresponding EELS elemental mapping images for f) Sr, g) Ti, and h) O, respectively. Line scans of i) Sr, j) Ti, and k) O elements refer to the position marked by the red line in (e).

the lattice distortion in the (001) plane of STO yields a spontaneous ferroelectric polarization normal to the (001)_{STO} plane. Consequently, the ferroelectric polarization direction of STO is perpendicular to the *c*-axis of TiO_2 and is in accordance with the charge-separation direction. The STEM image also demonstrates a typical core-shell heterostructures (Figure 2e). Corresponding EELS elemental mappings (Figure 2f-h) and line scans (Figure 2i-k) display the spatial arrangements of Sr, Ti, and O elements in a single NW. Obviously higher Sr signal

intensity was recorded along the NW edge, whereas both Ti and O exhibited a fairly uniform distribution across the entire NW body, confirming the TiO_2 -STO core-shell structure.

The TiO_2 and TiO_2 -STO NWs were then fabricated into PEC photoanodes with an exposed surface area of 0.25 cm². The water oxidation performance was evaluated in 1 M NaOH solution under the illumination of simulated AM 1.5 G solar light with a power density of 100 mW cm⁻². As shown in Figure 3a, the photocurrent density (J_{ph}) of the pristine TiO_2 NWs was 0.78 mA cm⁻² at 1.23 V versus the reversible hydrogen electrode (RHE), which is comparable to previously reported values.^[11,15,28] The TiO_2 -4.5 nm STO NWs yield a similar J_{ph} of 0.83 mA cm⁻² at 1.23 V versus RHE. When the STO thickness is increased to 10 nm, J_{ph} is substantially enhanced to 1.43 mA cm⁻² at 1.23 V versus RHE, corresponding to a 83% improvement over the pristine TiO_2 NWs. In addition to the J_{ph} , 10 nm thick STO shell can enable a better fill factor, implying more efficient charge separation and collection.^[3,11,28] The good fill factor and high saturated J_{ph} gave rise to an excellent applied bias photon-to-current efficiency of 0.85% at 0.49 V versus RHE (Figure S5, Supporting Information). Further increasing the STO thickness to 30 and 35 nm leads to a decrease of J_{ph} (1.32 and 1.28 mA cm⁻² at 1.23 V vs RHE, respectively). This deterioration was likely a result of the reduced surface area caused by the denser arrangement of NWs (Figure S2e,f, Supporting Information).

In principle, the J_{ph} is governed by three factors: light absorption, charge separation, and charge injection following the equation: $J_{\text{ph}} = J_{\text{abs}} \times \eta_{\text{separation}} \times \eta_{\text{injection}}$, where J_{abs} is the photocurrent density converted from the absorbed photons, $\eta_{\text{separation}}$ is the yield of the photogenerated surface-reaching holes, $\eta_{\text{injection}}$ is the yield of the surface-reaching holes that reacted with the electrolyte.^[29-31] To reveal the J_{ph} improvement, light absorption properties of TiO_2 and TiO_2 -STO NWs were first recorded by the UV-vis absorbance spectra (Figure 3b). Generally, their absorbance spectra exhibit similar behavior within the UV and visible light regions. The integrated light absorption values over 300–420 nm were 83.3%, 80.5%, 82.3%, 82.9%, and 83.2% for the TiO_2 and TiO_2 -STO NWs with STO thickness of 4.5, 10, 30, and 35 nm, respectively (Figure S6, Supporting Information). Assuming 100% internal quantum efficiency, the maximum achievable electron flux of the photoanodes can be estimated through integrating the absorbance across the AM 1.5 G solar spectrum (Figure S6, Supporting Information).

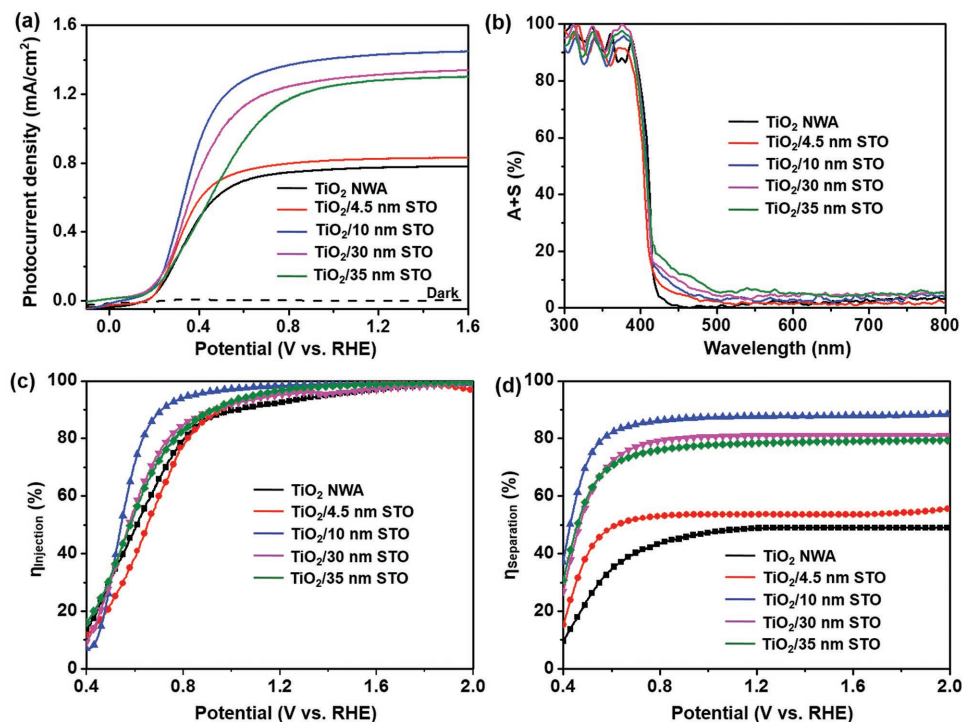


Figure 3. PEC performance characterization of TiO₂-STO core-shell NW-based photoanodes. a) Photocurrent-potential (J - V) curves of pristine TiO₂ NW arrays and TiO₂-STO core-shell NW arrays with different STO thickness (4.5, 10, 30, and 35 nm) measured in a 1 M NaOH solution (pH = 13.6) under AM 1.5 G illumination (100 mW cm⁻²). b) UV-visible absorption of pristine TiO₂ and all TiO₂-STO core-shell NW array samples. c) Charge injection efficiencies and d) charge-separation efficiencies of pristine TiO₂ and all TiO₂-STO core-shell NW array samples.

After integrating the electron flux within the wavelength range of 300–420 nm, the J_{abs} were determined to be 1.64, 1.55, 1.63, 1.64, and 1.65 mA cm⁻² for pristine TiO₂ and TiO₂-STO NWs with STO thickness of 4.5, 10, 30, and 35 nm, respectively. The variation of the J_{abs} is significantly smaller than the detected J_{ph} difference in Figure 3a, meaning the light absorption is not the dominating reason that caused the J_{ph} improvement.

To quantify the $\eta_{\text{injection}}$ and $\eta_{\text{separation}}$, J - V curves of sulfite oxidation were measured in a 0.5 M phosphate buffer containing 1 M sodium sulfite (pH = 7) under AM 1.5 G illumination (Figure S7, Supporting Information). PEC sulfite oxidation was a useful tool for assessing charge injection and separation properties of PEC materials due to the thermodynamically and kinetically more facile reaction process.^[29,32–34] The $\eta_{\text{injection}}$ and $\eta_{\text{separation}}$ can be calculated through comparing a series of photocurrent densities following the relationship $\eta_{\text{injection}} = J_{\text{ph}}/J_{\text{sulfite}}$ and $\eta_{\text{separation}} = J_{\text{sulfite}}/J_{\text{abs}}$, where J_{sulfite} is the photocurrent density for sulfite oxidation.^[29–31] Figure 3c,d presents the hole-injection and charge-separation yield for the TiO₂ and TiO₂-STO NWs. With the increase of STO film thickness, the $\eta_{\text{injection}}$ increased at first and then decreased in the low-bias region (<0.8 V vs RHE). TiO₂-10 nm STO delivered the highest $\eta_{\text{injection}}$ among all the five samples, implying an efficient interfacial hole injection from the STO surface to electrolyte in the low-bias region. At high-bias region (e.g., 1.23 V vs RHE), the $\eta_{\text{injection}}$ of all samples were around 90%, suggesting $\eta_{\text{injection}}$ was also not the reason of saturated J_{ph} variation. On the other hand, all TiO₂-STO NWs show higher $\eta_{\text{separation}}$ compared with pristine TiO₂ NWs (Figure 3d). The TiO₂-10 nm STO sample

accomplished the highest $\eta_{\text{separation}}$ of 87.7% at 1.23 V versus RHE, which was 79.3% improvement compared with pristine TiO₂ NWs (48.9% at 1.23 V vs RHE). The $\eta_{\text{separation}}$ improvement (79.3%) matched well with the J_{ph} increase (83.3%) for the TiO₂-10 nm STO NWs, suggesting $\eta_{\text{separation}}$ is the driving force of J_{ph} enhancement. The slightly-less-than-100% $\eta_{\text{separation}}$ might be attributed to the small energy discontinuity (0.32 meV, Figure S8, Supporting Information) or the existence of defects at the heterojunction between TiO₂ and STO.

In a PEC system, charge-separation efficiency is mainly determined by the width and amplitude of the depletion region in the photoactive semiconductor.^[30] STO shell substantially raised $\eta_{\text{separation}}$ which means the STO shell remarkably altered the electronic band bending of TiO₂. The likely charge source that caused this change is the ferroelectric polarization introduced by the lattice distortion of STO at the TiO₂-STO interface. To verify this hypothesis, we conducted the thermal treatment experiments and measured the polarization-electric field (P - E) hysteresis loops. For common heterojunctions, high-temperature annealing usually can improve the interface crystallinity. If other material properties (e.g., surface area and chemical composition) remain the same, which was likely the case in our system considering the identical NW morphology before and after annealing (Figure S9, Supporting Information), the better interface crystallinity could facilitate the charge transfer and enhance the PEC performance.^[35,36] Conversely, in our TiO₂-STO case, the J_{ph} and fill factors of the water oxidation curve drastically degraded after annealing the sample at 500 °C for 1 h (Figure 4a; and Figure S10, Supporting Information).

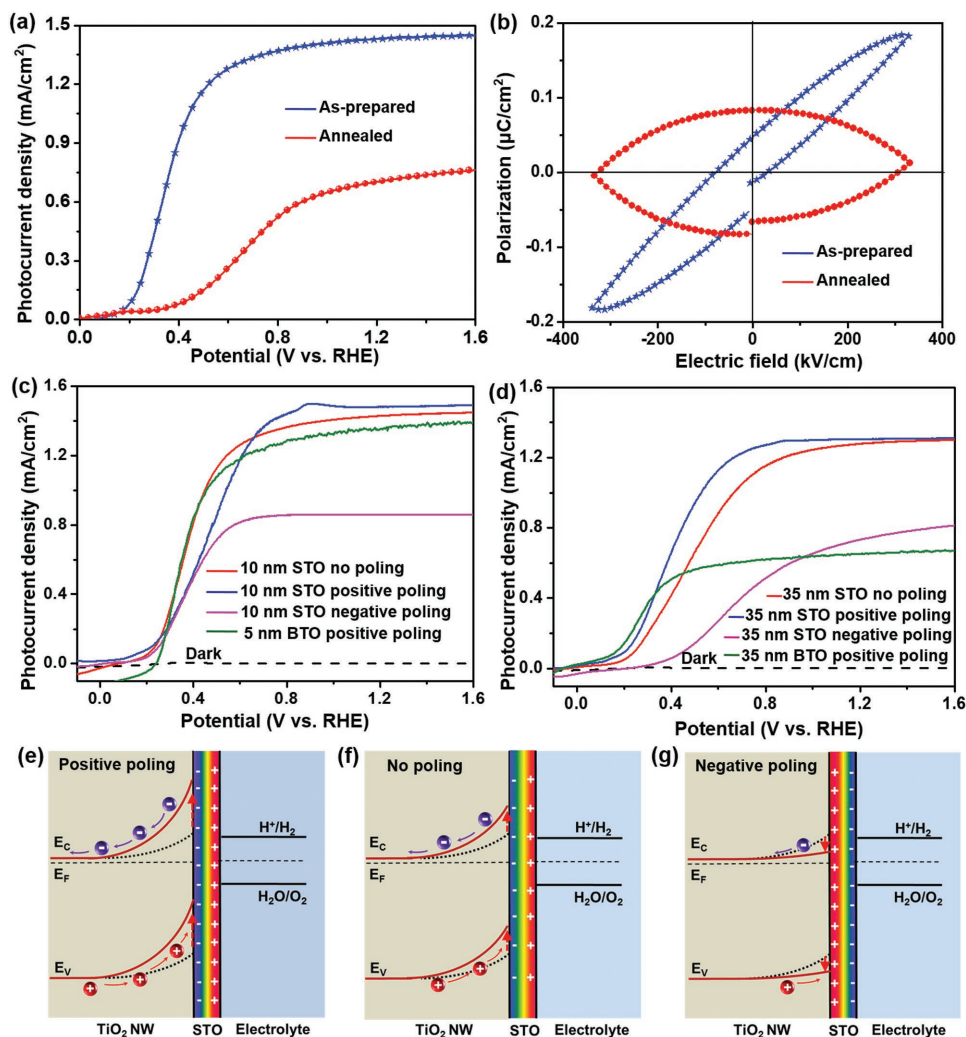


Figure 4. Ferroelectric polarization-related PEC performance characterization. a) Photocurrent–potential (J – V) curves measured from the TiO_2 /10 nm STO core–shell NW photoanode before (blue) and after (red) annealing at 500 °C for 1 h. b) Corresponding polarization–electric field hysteresis loops measured from the same samples before (blue) and after (red) annealing. c,d) J – V curves of the as-prepared (red), positively poled (blue), and negatively poled (magenta) TiO_2 /10 nm STO and d) TiO_2 /35 nm STO core–shell NW photoanodes and compared to positively poled (green) TiO_2 /BTO NW photoanodes. e–f) Schematic electronic band diagram of the TiO_2 –STO interface with e) positive poling, f) no poling, and g) negative poling conditions.

Figure 4b shows the P – E hysteresis loops of as-prepared and annealed TiO_2 –STO photoanodes at room temperature with an applied field of 400 kV cm^{-1} . The as-prepared TiO_2 –STO NWs exhibit a clear hysteresis P – E loop characteristic of ferroelectric materials with a saturation polarization (P_s) of $\approx 0.15 \mu\text{C cm}^{-2}$, remnant polarization (P_r) of $\approx 0.05 \mu\text{C cm}^{-2}$, and coercive field (E_c) of $\approx 78 \text{ kV cm}^{-1}$, evidencing the appreciable ferroelectricity of the as-prepared TiO_2 –STO NWs. After 500 °C annealing, the measured polarization was simply dominated by the leakage current and exhibited no ferroelectric behavior.^[37] This phenomenon was consistent with the well documented theory that high-temperature annealing was able to eliminate the ferroelectricity of STO by releasing the interface strain.^[35,38,39] The XRD characterization reveals that the rutile TiO_2 phase remain unchanged before and after the annealing (Figure S11, Supporting Information), excluding the possibility of TiO_2 -induced performance variation. These results suggest the removal of

STO ferroelectric polarization could give rise to the deterioration of the PEC performance, highlighting the key role of the STO ferroelectricity in improving the charge-separation and water-splitting performance of TiO_2 –STO NWs. After increasing the STO thickness to 35 nm, the P_s and P_r were increased to 0.65 and 0.18 $\mu\text{C cm}^{-2}$, respectively (Figure S12, Supporting Information). It should be noted that both P – E loops from the 10 and 35 nm STOs exhibited a considerable leakage. The leakage was likely associated with the high electron conductivity of STO, which was favorable for the PEC applications where charge transport was also an essential factor.

Similar with other ferroelectric PEC systems (e.g., TiO_2 –BTO photoelectrode), the PEC performance of TiO_2 –STO NWs can be effectively tuned by external bias. As shown in Figure 4c,d, positive poling (i.e., positive voltage was applied on the fluorine-doped tin oxide (FTO) substrate, see the Experimental Section for details) can further improve J_{ph} of TiO_2 10 and 35 nm

STO NWs as a result of the enhanced ferroelectric polarization. The relatively small improvement amplitude suggests the spontaneous ferroelectric polarization in the STO shell is mostly aligned in the favorable direction (i.e., positive poling direction). As shown in Figure 4e,f, under this polarization, negative ferroelectric charge will present at the TiO₂-STO interface and amplify the band bending of TiO₂, which eventually enhance the charge separation and photocurrent density. In contrast, negative poling will switch the polarization direction and reduce the depletion width of TiO₂ (Figure 4g), resulting in a substantial decrease of J_{ph} . A similar change trend of J_{ph} responding to poling treatment was also observed for the TiO₂ 4.5 and 30 nm STO NWs (Figure S13, Supporting Information). Compared to TiO₂-BTO ferroelectric PEC system, the unique advantage of STO is its good charge mobility, which will facilitate the hole migration inside the ferroelectric layer. This hypothesis was verified by the hall measurement, which reveals that the electron mobility of TiO₂/10 nm STO and TiO₂/5 nm BTO heterostructures are 3.4 and 0.8 cm² V⁻¹ s⁻¹, respectively. Therefore, the saturated J_{ph} of TiO₂ 10 nm STO NWs was 1.1 times higher than that of the TiO₂ 5 nm BTO NWs (Figure 4c). When using thicker ferroelectric layer (35 nm), the discrepancy of the saturated J_{ph} between TiO₂-STO and TiO₂-BTO was raised to 101.5% since the hole-migration impedance is more conspicuous (Figure 4d). The data of TiO₂-BTO were collected following the previous report,^[25] which were prepared through the same procedure. In addition to thermal annealing and electrical poling, other promising methods to control the ferroelectric polarization of STO include straining the crystal lattice of STO and engineering the interfacial chemistry of TiO₂-STO.

In summary, we developed a ferroelectric-enhanced PEC system by hydrothermally converting TiO₂ NW surface to STO with controllable film thickness. Compared to pristine TiO₂ NWs, the TiO₂-STO NWs exhibited significantly improved PEC water-splitting performance under AM 1.5 G illumination. The highest J_{ph} (1.43 mA cm⁻² at 1.23 V vs RHE) and $\eta_{separation}$ (87.7% at 1.23 V vs RHE) were accomplished with \approx 10 nm thick STO shell, which were 83% and 79% higher than those of bare TiO₂ NWs. The origin of the remarkable improvement in PEC performance was attributed to the ferroelectric polarization-induced upward band bending of the TiO₂ core, which effectively drove the separation and transport of photogenerated charge carriers. Compared to other ferroelectric PEC system such as TiO₂-BTO NWs, the good charge mobility of STO largely reduces the hole-transporting impedance and thus favors the photocurrent density. This work demonstrates that appropriate combination of ferroelectric polarization and charge transport in a semiconducting ferroelectric material, e.g., STO, could be a superior solution to PEC performance improvement instead of using insulating ferroelectric materials. This strategy will find broad application potentials for further advancing the performance in piezotronics-regulated semiconductor systems such as photovoltaic devices, sensors, light emitting diodes, and electrochemical electrodes.

Experimental Section

Hydrothermal TiO₂ NW Array Growth: Rutile TiO₂ NW arrays were grown on the FTO via hydrothermal methods according to a reported

procedure.^[40] First, dense TiO₂ blocking layer was spin-coated on a clean FTO surface with a speed of 5000 revolutions per minute (r.m.p.) for 30 s using a solution containing 20 μ L of 37% HCl and 0.7 mL of titanium (IV) tetraisopropoxide (TTIP) in 10 mL ethanol. Afterward, the substrate was annealed at 500 °C for 1 h in air. The FTO substrate was then loaded into a sealed Teflon-lined stainless-steel autoclave filled with 10 mL of 37% HCl, 10 mL of deionized water and 0.20 mL of TTIP following by heating at 170 °C for 4 h. After cooling down to room temperature, the resulting TiO₂ NWs on FTO substrates were rinsed with deionized water and subsequently annealed at 500 °C for 1 h in air. The TiO₂ NW arrays preferentially grew on the compact TiO₂ blocking layer of FTO substrates.

Synthesis of the TiO₂-SrTiO₃ Core-Shell NW Arrays: TiO₂-SrTiO₃ core-shell NWs were prepared from the rutile TiO₂ NWs by a second hydrothermal conversion reaction in aqueous strontium hydroxide octahydrate solution. During the typical synthesis, the TiO₂ NWs were immersed in a sealed Teflon-lined stainless-steel autoclave loaded with solutions of Sr(OH)₂·8H₂O (0.5 mmol) in 5 mL of diethylene glycol, 5 mL of ethanol, 1.5 mL 2-propanol, 0.5 g of tetrabutylammonium hydroxide solution (TBAH, 40 wt%), and 7 mL of deionized water and heated at 160 °C for 1–4 h. The obtained products were washed with deionized water and ethanol, and dried in air.

Characterization: X-ray diffraction patterns were acquired from the Rigaku D/max-2200V diffractometer with Cu K _{α} radiation. SEM measurements were performed on JEOL JSM-6700F field-emission microscopes and TEM measurements were done on JEOL JEM-2010F microscopes. STEM and EELS experiments were performed on a FEI Titan microscope with a CEOS probe aberration-corrector operated at 200 keV. The absorption spectra were recorded using an Evolution 220 UV-vis spectrophotometer with integrated sphere (ISA 220). The *P*-*E* hysteresis loops were performed using a ferroelectric measurement system (Precision Premier Workstation, Radiant Technologies, Palo Alto, CA, USA) at room temperature. For the hall measurement, a dense TiO₂ layer was spin-coated on a quartz surface, and heated at 700 °C for 4 h, yielding a 50 nm thick rutile TiO₂ film on the quartz substrate. After that, 10 and 5 nm thick STO were prepared by converting the 50 nm thick rutile TiO₂ layer in Sr(OH)₂ and Ba(OH)₂ solution at 160 and 150 °C for 2 h, respectively. At last, four Pt electrodes were deposited by thermal evaporation for the contact purpose.

PEC Measurement for Water Splitting: The PEC measurements were carried out in a quartz cell using a typical three-electrode system with the TiO₂ and TiO₂-SrTiO₃ NWs as the working electrode, Pt foil as the counter electrode, and a saturated calomel electrode (SCE) as the reference electrode. The SCE is converted to RHE using the equation: $E(\text{RHE}) = E(\text{SCE}) + 0.241 \text{ V} + 0.059 \times \text{pH}$. The electrolyte was a 1 M NaOH aqueous solution (pH 13.6). Light irradiation was provided by a solar simulator (Newport) coupled with AM 1.5 G filter. The potential was scanned from -1.5 to 1.0 V versus SCE at a rate of 50 mV s⁻¹. The Poling experiment was conducted through a sandwich structure with FTO glass (top electrode)/sample NWs on FTO substrate glass (bottom electrode) at room temperature for 10 min. The poling voltage was \pm 10 V. Positive poling was applying positive potential to the bottom FTO electrode.

Supporting Information

Supporting Information is available from the Wiley Online Library or from the author.

Acknowledgements

F.W. and Y.H.Y. contributed equally to this work. This work was supported by National Science Foundation under Award No. CMMI-1148919. W.Y. thanks the financial support from the National Science Foundation of China (No. 51202139).

Conflict of Interest

The authors declare no conflict of interest.

Keywords

ferroelectric polarization, piezotronics, photoelectrochemical water splitting, SrTiO₃, TiO₂ nanowires

Received: March 14, 2017

Revised: April 23, 2017

Published online:

-
- [1] A. Fujishima, K. Honda, *Nature* **1972**, 238, 37.
 [2] M. Gratzel, *Nature* **2001**, 414, 338.
 [3] M. G. Water, E. L. Warren, J. R. McKone, S. W. Boettcher, Q. Mi, E. A. Santori, N. S. Lewis, *Chem. Rev.* **2010**, 110, 6446.
 [4] Y. Yu, Z. Zhang, X. Yin, A. Kvit, Q. Liao, Z. Kang, X. Yan, Y. Zhang, X. Wang, *Nat. Energy* **2017**, 2, 17045.
 [5] A. L. Linsebigler, G. Q. Lu, J. T. Yates, *Chem. Rev.* **1995**, 95, 735.
 [6] P. V. Kamat, *Chem. Rev.* **1993**, 93, 267.
 [7] H. A. Atwater, A. Polman, *Nat. Mater.* **2010**, 9, 205.
 [8] Y. Yu, X. Yin, A. Kvit, X. D. Wang, *Nano Lett.* **2014**, 14, 2528.
 [9] K. Shankar, J. I. Basham, N. K. Allam, O. K. Varghese, G. K. Mor, X. Feng, M. Paulose, J. A. Seabold, K.-S. Choi, C. A. Grimes, *J. Phys. Chem. C* **2009**, 113, 6327.
 [10] G. K. Mor, K. Shankar, M. Paulose, O. K. Varghese, C. A. Grimes, *Nano Lett.* **2005**, 5, 191.
 [11] I. S. Cho, Z. Chen, A. Forman, D. R. Kim, P. M. Rao, T. F. Jaramillo, X. Zheng, *Nano Lett.* **2011**, 11, 4978.
 [12] S. G. Kumar, L. G. Devi, *J. Phys. Chem. A* **2011**, 115, 13211.
 [13] C. Liu, J. Tang, H. M. Chen, B. Liu, P. Yang, *Nano Lett.* **2013**, 13, 2989.
 [14] Y. J. Hwang, C. Hahn, B. Liu, P. Yang, *ACS Nano* **2012**, 6, 5060.
 [15] I. S. Cho, C. H. Lee, Y. Feng, M. Logar, P. M. Rao, L. Cai, D. R. Kim, R. Sinclair, X. Zheng, *Nat. Commun.* **2013**, 4, 1723.
 [16] M. Xu, P. Da, H. Wu, D. Zhao, G. Zheng, *Nano Lett.* **2012**, 12, 1503.
 [17] T. Choi, S. Lee, Y. J. Choi, V. Kiryukhin, S.-W. Cheong, *Science* **2009**, 324, 63.
 [18] I. Grinberg, D. V. West, M. Torres, G. Gou, D. M. Stein, L. Wu, G. Chen, E. M. Gallo, A. R. Akbashev, P. K. Davies, J. E. Spanier, A. M. Rappe, *Nature* **2013**, 503, 509.
 [19] J. Hoffman, X. Pan, J. W. Reiner, F. J. Walker, J. P. Han, C. H. Ahn, T. P. Ma, *Adv. Mater.* **2010**, 22, 2957.
 [20] W. Yang, Y. Yu, M. B. Starr, X. Yin, Z. Li, A. Kvit, S. Wang, P. Zhao, X. Wang, *Nano Lett.* **2015**, 15, 7574.
 [21] Z. Wang, D. Cao, L. Wen, R. Xu, M. Obergfell, Y. Mi, Z. Zhan, N. Nasori, J. Demsar, Y. Lei, *Nat. Commun.* **2016**, 7, 10348.
 [22] Y. Yuan, T. J. Reece, P. Sharma, S. Poddar, S. Ducharme, A. Gruverman, Y. Yang, J. Huang, *Nat. Mater.* **2011**, 10, 296.
 [23] J. Hoffman, X. Pan, J. W. Reiner, F. J. Walker, J. P. Han, C. H. Ahn, T. P. Ma, *Adv. Mater.* **2010**, 22, 2957.
 [24] J. H. Haeni, P. Irvin, W. Chang, R. Uecker, P. Reiche, Y. L. Li, S. Choudhury, W. Tian, M. E. Hawley, B. Craigo, A. K. Tagantsev, X. Q. Pan, S. K. Streiffer, L. Q. Chen, S. W. Kirchoefer, J. Levy, D. G. Schlom, *Nature* **2004**, 430, 758.
 [25] J. H. Lee, A. Selloni, *Phys. Rev. Lett.* **2014**, 112, 196102.
 [26] M. S. Wrighton, A. B. Ellis, P. T. Wolczanski, D. L. Morse, H. B. Abrahamson, D. S. Ginley, *J. Am. Chem. Soc.* **1976**, 98, 2774.
 [27] R. Marschall, *Adv. Funct. Mater.* **2014**, 24, 2421.
 [28] X. J. Feng, K. Shankar, O. K. Varghese, M. Paulose, T. J. Latempa, C. A. Grimes, *Nano Lett.* **2008**, 8, 3781.
 [29] T. W. Kim, K.-S. Choi, *Science* **2014**, 343, 990.
 [30] H. Dotan, K. Sivula, M. Gratzel, A. Rothschild, S. C. Warren, *Energy Environ. Sci.* **2011**, 4, 958.
 [31] M. Zhou, J. Bao, W. Bi, Y. Zeng, R. Zhu, M. Tao, Y. Xie, *ChemSusChem* **2012**, 5, 1420.
 [32] X. Shi II, Y. Choi, K. Zhang, J. Kwon, D. Y. Kim, J. K. Lee, S. H. Oh, J. K. Kim, J. H. Park, *Nat. Commun.* **2014**, 5, 4775.
 [33] H. Ye, J. Lee, J. S. Jang, A. J. Bard, *J. Phys. Chem. C* **2010**, 114, 13322.
 [34] Y.-S. Chen, J. S. Manser, P. V. Kamat, *J. Am. Chem. Soc.* **2015**, 137, 974.
 [35] L. Li, G. S. Rohrer, P. A. Salvador, *J. Am. Ceram. Soc.* **2012**, 95, 1414.
 [36] Y. Sun, K. Yan, G. Wang, W. Guo, T. Ma, *J. Phys. Chem. C* **2011**, 115, 12844.
 [37] Z. Fan, J. Xiao, K. Sun, L. Chen, Y. Hu, J. Ouyang, K. P. Ong, K. Zeng, J. Wang, *J. Phys. Chem. Lett.* **2015**, 6, 1155.
 [38] L. Li, J. Briston, J. R. Jokisaari, Y. Zhang, C. Adamo, A. Melville, D. G. Schlom, L.-Q. Chen, X. Pan, *Adv. Mater.* **2016**, 28, 6562.
 [39] S. Y. Yang, J. Seidel, S. J. Byrnes, P. Shafer, C.-H. Yang, M. D. Rossell, P. Yu, Y.-H. Chu, J. F. Scott, J. W. Ager, L. W. Martin, R. Ramesh, *Nat. Nanotechnol.* **2010**, 5, 143.
 [40] B. Liu, E. S. Aydil, *J. Am. Chem. Soc.* **2009**, 131, 3985.